Design of a Power-Dense Aviation Motor With a Low-Loss Superconducting Slotted Armature

Runar Mellerud, Christian Hartmann, Casper Leonard Klop, Sindre Austad, and Jonas Kristiansen Nøland, *Senior Member, IEEE*

***Abstract*—This article describes the design and analysis of a 2.5-MW, 5000-r/min electric motor with a slotted armature employing rare-earth barium copper oxide (REBCO) high-temperature superconductors (HTS). The alternating current and field in the armature induces ac losses in the superconductors, requiring cryogenic cooling. Therefore, the aim is to design a machine with sufficiently low losses to make this cooling realistic, which simultaneously outperforms the state-of-the-art. The reasoning behind the key design choices is presented before the model used for 2-D finite element analysis (FEA) is described. Then, HTS ac losses are studied with the T-A-formulation, examining the impact of various operating conditions. Aligning the HTS tapes with the field was found to successfully reduce ac losses, while filamentization was only successful for more than ten filaments. The final design had an active torque density of 50.9 N·m/kg and an estimated efficiency of 99.8% when the HTS are operated at 40 K.**

***Index Terms*—AC loss, armature superconducting, aviation motor, filaments, finite element analysis (FEA), high-temperature superconductors (HTS), Rare-earth barium copper oxide (REBCO), Roebel cables.**

I. Introduction

MOST of the climate impact from the aviation sector is not caused by CO_2, but contrails and NOx, produced by the high temperatures required in combustion engines [1]. Electrically powered fans or propellers can avoid these emissions altogether, and the development of fully electric or fuel cell electric powertrains is required for a true zero-emission scenario. Nevertheless, it has proven a challenge to design electric components meeting the extreme weight and efficiency requirements posed by the aviation sector.

Rare-earth barium copper oxide (REBCO) coated conductors can carry high currents and could potentially enable compact and lightweight electric machines even at direct-drive speeds. Also, their low losses give an extremely high efficiency, reducing the power and energy requirements and, thereby, the weight of other powertrain components. These properties have caused high-temperature superconductors (HTS) to be considered a key enabler for electric aviation [2]. However, HTS experience ac losses when exposed to alternating currents and magnetic fields, and a complex cooling system with high cooling penalties is required to maintain cryogenic temperatures [3]. Because of this, it is still unclear whether ac losses in an HTS armature compromise the machine benefits [4]. For example, Haran et al. [5] argued that losses in a superconducting armature must be significantly less than 0.1% of the machine's rated power to be competitive with its alternatives. Even higher losses could be tolerated if using liquid hydrogen (LH_2) fuel as a cryogenic heat sink [6], but also this has a limited cooling capacity [7].

The recent development of the mixed **T-A**-formulation has enabled accurate ac loss estimations with low computation times [8], making it a powerful tool in the design of electric machines with a large number of HTS tapes [9], [10], [11], [12]. Although aviation machines with HTS armatures have been explored in multiple previous papers [13], [14], [15], [16], [17], [18], [19], [20], [21], none have conducted a detailed finite element analysis (FEA) of ac losses in a power-dense full-scale aviation motor. In this article, the **T-A**-formulation is therefore used to explore the potential of a $2.5\,\mathrm{MW}$ aviation motor with a slotted stator and HTS armature windings, while assessing its feasibility with respect to cryogenic cooling requirements. This is done through a comprehensive ac loss analysis, studying special HTS design considerations, as well as the impact of multiple design modifications and loss mitigation methods. Finally, the design is compared with the state-of-the-art (SotA) within power-dense conventional machines.

The rest of this article is organized as follows. Section II gives an overview of the machine design choices, followed by the FEA modeling approach and material properties in Section III. In Section IV, the HTS ac losses are studied for several operating conditions and loss reduction methods. In Section V, the key machine parameters are presented and are used together with results from the HTS analysis to evaluate the design relative to the SotA, while discussing the implications of the results. Finally, Section VI concludes this article.

II. Electrical Machine Design

Before presenting the analysis part of this article, the description of the machine design will be provided as a foundation, explaining the reasoning behind the key design choices, focusing

Manuscript received 30 June 2023; revised 24 August 2023; accepted 12 September 2023. Date of publication 18 September 2023; date of current version 3 October 2023. *(Corresponding author: Runar Mellerud).*

Runar Mellerud, Casper Leonard Klop, Sindre Austad, and Jonas Kristiansen Nøland are with the Department of Electric Energy, Norwegian University of Science and Technology (NTNU), 7491 Trondheim, Norway (e-mail: runar.mellerud@ntnu.no).

Christian Hartmann is with the Institute for Energy Technology, 1777 Halden, Norway, and also with the Department of Electric Energy, Norwegian University of Science and Technology (NTNU), 7491 Trondheim, Norway.

Color versions of one or more figures in this article are available at https://doi.org/10.1109/TASC.2023.3316192.

Digital Object Identifier 10.1109/TASC.2023.3316192

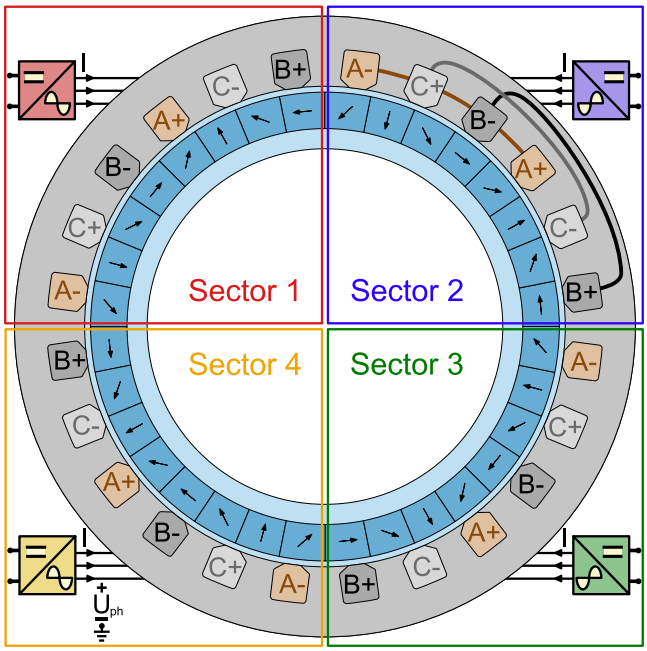

Fig. 1. Overview of the machine design, where the armature is divided into four separate sectors, each connected to its own converter module. The arrows in the Halbach array rotor magnets indicate their magnetization direction.

TABLE I
MACHINE'S GEOMETRICAL PARAMETERS

Parameter	Symbol	Value	Unit
Number of slots	N_s	24	
Number of poles	N_p	8	
Outer diameter	D_o	346	mm
Air gap diameter	D_{ag}	260	mm
Active length	l_a	240	mm
Air gap length	g	4	mm
Magnet length	l_m	20	mm
Slot opening width	w_{so}	8	mm
Slot opening height	h_{so}	1	mm
Height to useful slot	h_1	5	mm
Useful slot height	h_{us}	17	mm
Slot width	w_s	20	mm
Stator core material	0.2 mm vacoflux 50		
PM material	NdFeB BMN-46EH (GBD)		

on machine topology, HTS coil design, and the envisioned cooling method.

A. Investigated Machine Design

An overview of the machine design is shown in Fig. 1, with parameters given in Table I. The machine has 24 slots and eight poles and a distributed winding layout with a coil span of three slots. This layout has four symmetrical sectors, where each can be coupled to its separate converter module. This technique is described as functional modularity and allows each module to be operated separately from the others, introducing redundancy in the drive design [22]. In the case of a fault in one module, it can be switched OFF, allowing the machine to continue operation at a reduced output. Furthermore, the parallel coupling of four converters helps keep the voltage at a manageable level.

A high-current loading in the armature winding is required to ensure a high power density. However, the high armature current introduces a nonnegligible slot leakage flux, meaning that the slots are not entirely successful in protecting the superconductors from alternating magnetic fields [23]. Nevertheless, a slotted armature can be designed to shield HTS more from magnetic fields than a slotless one; careful design of the slot shape can keep the slot field amplitude relatively low and also almost unidirectional, making it easy to align the HTS tapes with the field, largely avoiding Eddy currents from the perpendicular field component. Since the field will be mostly in the tangential direction, the HTS must be placed almost flat in the slot, ruling out the typical racetrack coil since it has out-of-plane bent HTS, which would be perpendicular to the field. In-plane bending of HTS is both difficult and could lead to irreversible damage, and a saddle-like coil could be necessary. A saddle-like type of coil is well suited for the chosen winding layout. Finally, Lorentz forces are less of a problem in a slotted design since they will point into the slot.

A four-segment permanent magnet (PM) Halbach array without back-iron was chosen for the rotor magnetization. This is a mature solution offering a near sinusoidal flux distribution [24], a high power density [25], and could also be designed for low losses through axial magnet segmentation [26]. Furthermore, the design study of Corduan et al. [14] suggested that in a fully superconducting machine, the preferable air gap flux density is between 0.55–$0.9\,\text{T}$, well within the range of NdFeB magnets. While the thermal stability of NdFeB-magnets is worse than that of SmCo, a machine with an HTS armature will have a negligible stator-to-rotor heat leak, making it easier to maintain a low temperature. Also, with grain boundary diffusion (GBD), the coercivity of these magnets can be increased, reducing the risk of irreversible demagnetization. A nonmagnetic material is assumed to support the array on the inside, while a retention sleeve on the outside holds the magnets in place. Based on centrifugal force estimations, an air gap of $4\,\text{mm}$ was found sufficient to fit the sleeve with room to spare. The magnet length of $20\,\text{mm}$ gave an average air gap flux of $0.77\,\text{T}$ at full load. The rotor is representative of these types of machines, and since the main focus of this study has been to investigate HTS armature losses, it has not been sought to optimize the rotor geometry or investigate HTS field windings [27].

B. HTS Coil Design

To reduce insulation requirements, the phase voltage was restricted to a maximum of $500\,\text{V}$, meaning that the number of turns must be limited. Consequently, to get the desired power output, each turn must carry a high current, and multiple superconductors must be coupled in parallel. With a substantial slot leakage flux, the parallel conductors must be transposed to avoid large circulating currents within the stack. Alternatively, all strands could be insulated with a thin layer of polyimide/Kapton and be parallel coupled at the very ends. However, this would not only insulate the conductors electrically but also thermally, making cooling more difficult. In addition, it would require more slot space.

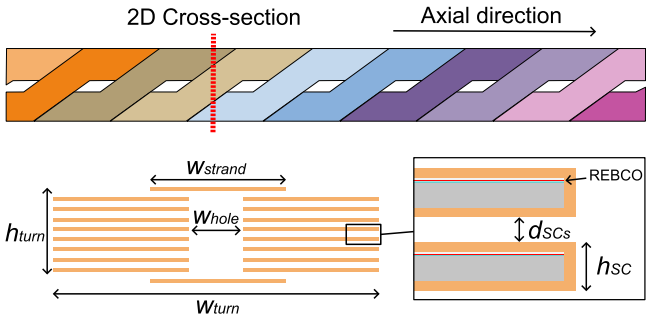

Fig. 2. Illustration of one turn of REBCO Roebel cable with the modeled 2-D section. Only the REBCO layer is modeled in the HTS loss analysis in the form of an infinitely thin strip.

TABLE II
HTS COIL PARAMETERS

Parameter	Symbol	Value	Unit
Critical current @40 K, s.f.	$I_{c,40K,\text{s.f.}}$	2543	A/cm
REBCO-layer thickness	δ	1	µm
HTS tape thickness	h_{SC}	80	µm
Distance between SC-strands	d_{SCs}	0	µm
Superconductor strand width	W_{strand}	1.9	mm
Center hole width	W_{hole}	0.2	mm
Turn width	W_{turn}	4	mm
Turn height	h_{turn}	0.8	mm
Vertical distance between turns	d_{turns}	0.5	mm
Coil height	h_{coil}	8.6	mm
Strands per turn	N_{strands}	18	
Number of turns	N_{turns}	14	
HTS material	Shanghai SC LFHT [31]		

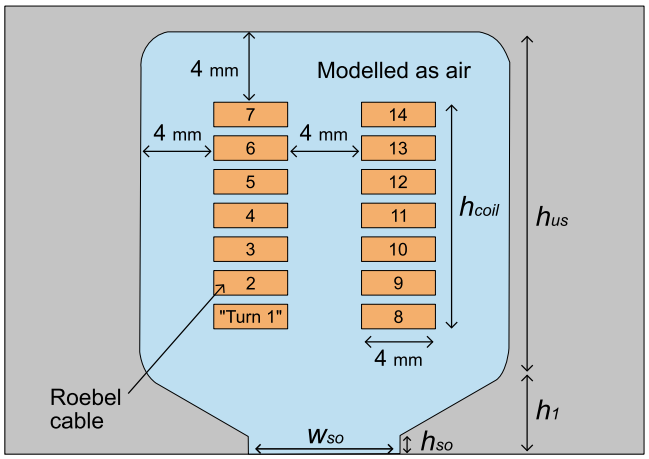

Fig. 3. Sketch of slot layout with parameters for the HTS coil and slot geometry. The turns are numbered for discussion of the results.

Because of the high aspect ratio of the HTS tapes, there are limited ways, in which transposition can be done effectively. For this purpose, the Roebel cable has been shown to be manufacturable for HTS through a punching technique [28], [29]. This configuration transposes the conductors along the axial direction of the electric machine, illustrated in Fig. 2. As shown in the same figure, this work considers the 2-D cross section of the Roebel cable in the middle of a transposition both on the top and bottom of the cable. This cross-section should give slightly higher losses than one where all conductors are side-by-side [30]. Due to the transposition, the current is assumed to be evenly distributed between the strands.

The Roebel cable geometry was based on the work by Otten [32], with tightly packed $1.9\,\text{mm}$ wide strands without inter-strand insulation. Otten's ten-strand cable had a transposition length of $116\,\text{mm}$. In this article, 18 parallel strands are assumed, and the active length of $240\,\text{mm}$ is considered sufficient to fit one full transposition. The HTS tape thickness is set to 80 μm, and a $0.5\,\text{mm}$ vertical distance between each turn is reserved for electric insulation and mechanical clearance. Fig. 3 shows the resulting coil and slot layout, with parameters given in Tables I and II.

C. Cryogenic Cooling System

While not the main focus of this article, the cryogenic cooling system will have a significant impact on the machine layout and the resulting power density. Therefore, a few design considerations are discussed in this section.

To provide cryogenic cooling, mainly two options are envisioned: cryocoolers and/or dual use of LH_2 as fuel and coolant [33]. As shown in this article, an HTS armature will have cold losses in the kW range. A cryocooler consumes a substantial amount of power to remove heat at cryogenic temperatures (cooling penalty). Using optimistic cryocooler performance estimations from Felder et al. [34], removing $1\,\text{kW}$ of losses at $40\,\text{K}$ would result in a cryocooler requiring $21.6\,\text{kW}$ of input power and weighing $64.8\,\text{kg}$. Hence, using a cryocooler to provide the main cooling power does not seem like a viable option for this machine. On the other hand, an LH_2 cooling loop running through the whole superconducting propulsion system has a promising potential [6]. Such a system was studied by Hartmann et al. [7], showing that the cryogenic cooling capacity of LH_2 is more than enough to cool kW-scale losses at cryogenic temperatures. Nevertheless, the authors are not aware of a detailed design of such a cryocooling circuit.

Several cooling concepts for superconducting armatures have been proposed in the literature. Broadly speaking, they can be grouped into designs with either a cryogenic or a warm stator core. A cryogenic stator core can be achieved by cooling channels in the slots and/or yoke. Cooling channels in the yoke enable a simpler cooling system, and a cold steel would require no thermal insulation in the slot. The primary downside with this solution is that in addition to the coil losses, the steel losses would also need to be dissipated into the coolant. The alternative is to keep the stator steel warm by thermally insulating the HTS coils from the steel core. This can be achieved by a vacuum gap [14], a cryostat [35], or thermal insulation. In this article, the last option is assumed since it is easier to realize for a slotted stator.

A first-order calculation shows that if a material similar to closed-cell polyurethane, considered for LH_2 tanks [36], can be used for slot insulation, the heat leakage into the slot is manageable. A sketch of this concept is shown in Fig. 4. With a thermal conductivity of $0.01\,\text{W}/\text{mK}$, $3\,\text{mm}$ of insulation results

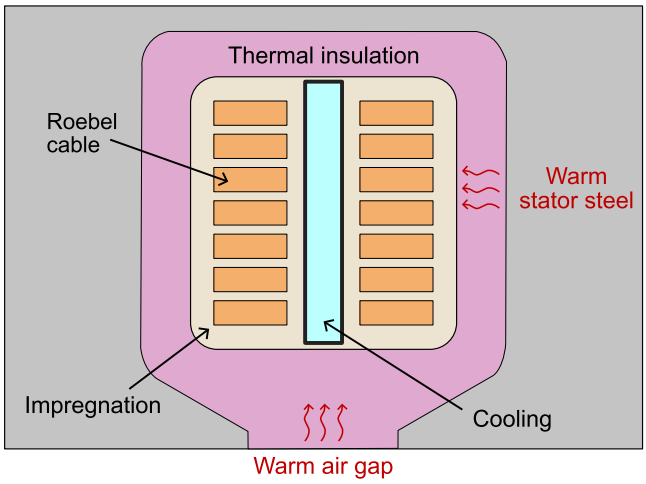

Fig. 4. Conceptual sketch of the outlined cooling solution.

in a heat leak of 16 W per slot for a 250 K difference between slot and stator iron. This is less than the HTS ac loss per slot, as will be discussed later. The downsides of this concept become clear from Fig. 4 as well. The thick insulation layer will lead to a low slot fill factor, partially canceling the benefit of a high current density gained by using superconductors in the stator. Furthermore, foams, such as polyurethane, have low strength and are likely unable to withstand forces from the HTS coils, and mechanical reinforcements might be required within the slot.

The electrical insulation and impregnation of the coils could also pose a challenge related to keeping the HTS cooled since it will act as a thermal barrier [37]. When using many different materials within the slot, thermal contraction must also be considered. For now, the slot layout is assumed to be feasible, but further research is required to investigate whether this is the case.

III. Finite Element Modeling

In this work, 2-D FEA is conducted with COMSOL multiphysics to analyze the machine performance and the HTS ac losses. This section describes the modeling approach along with the implemented material properties.

A. FEA Machine Model

Symmetry allowed the FEA machine model to be reduced to a sector with one pole, three slots, and antiperiodic boundary conditions. As illustrated in Fig. 5, two models were used. A basic model with only the A-formulation and lossless coils was used for the initial design and to analyze the machine's performance. A separate model was made to analyze the HTS ac losses, where the **T-A**-formulation was implemented on the superconductors in one slot only (i.e., phase B+) since losses in the other slots are equal but phase-shifted due to symmetry. Both models have a pure q-axis current to obtain maximum torque per ampere.

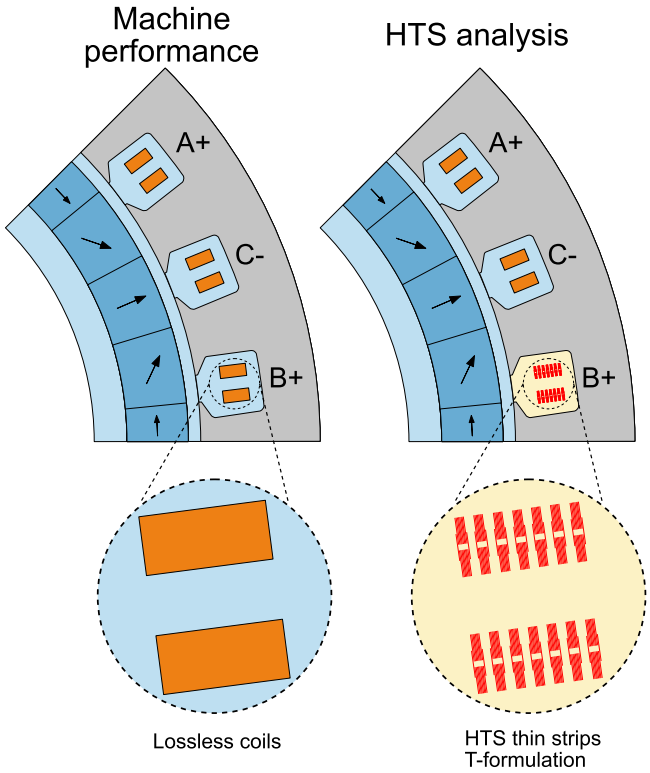

Fig. 5. Machine models used in the analysis. All results except HTS losses were obtained from the model with lossless coils. In the right model, all is equal except for applying the T-formulation on infinitely thin strips in one slot.

B. Steel and Magnet Material Properties

The BH-curve of vacoflux 50 was applied for the electrical steel in all analysis. Its material properties were imported from the COMSOL library. Vacoflux 50 saturates at a magnetic flux of approximately 2.3 T, allowing for minimal steel volume for a given magnetic loading. Characteristic data obtained from 0.2 mm thick Vacoflux 50 was used to obtain loss coefficients in the steel loss estimation. For the PMs, COMSOL data of the NdFeB BMN-46EH (GBD) was implemented. At 20 °C, this material has a remanent flux density of about 1.38 T.

C. HTS Material Properties

The superconductor resistivity, ρ_{HTS}, was modeled through the E-J power-law with field-dependent critical current density J_c, and power-law index n

$$\rho_{\mathrm{HTS}} = \frac{E_c}{J_c(\mathbf{B}_{\mathrm{ext}})}\left(\frac{|J|}{J_c(\mathbf{B}_{\mathrm{ext}})}\right)^{n(\mathbf{B}_{\mathrm{ext}})-1} \tag{1}$$

where $E_c = 1\ \mu$V/cm is the defined critical electric field, $\mathbf{B}_{\mathrm{ext}}$ is the external magnetic field, and J is the current density. To model the field dependency of the critical current and the power-law index, anisotropic Kim-like models [39], [40] were fit on data from the Robinson database [38] for the Shanghai superconductor low-field, high-temperature 2G HTS [31]. The resulting curve fits at 40 K are plotted in Fig. 6 together with the input data. Due to the curve shape of n's field dependency, it was difficult to make an accurate curve fit for it. Still, n is often

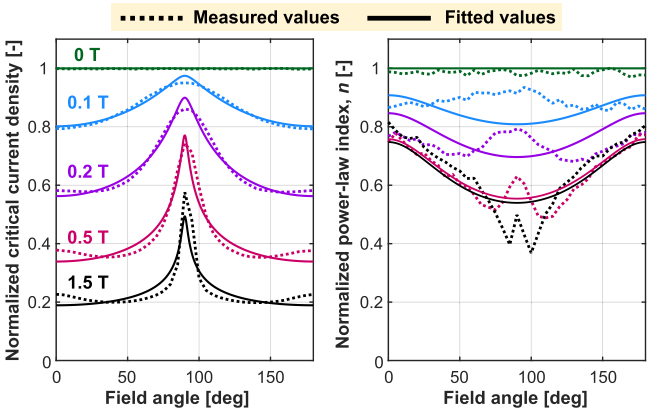

Fig. 6. HTS curve fits at 40 K for critical current density (left-hand side) and power-law index, n (right-hand side), based on measured data from the Robinson database [38] and normalized with respect to self-field values. The color coding is equal for both. A 90° field is parallel with the tapes.

assumed to be constant since it impacts the losses far less than the critical current density. Therefore, the curve fit was considered adequate for this analysis.

At 40 K, the self-field critical current per width for this superconductor is about $2543\,\mathrm{A/cm}$, while the self-field power-law index is approximately 27.2. For the analysis of ac loss temperature dependency, similar curve fits were made for 25, 30, 50, and 60 K.

D. HTS Finite Element Modeling

The **T-A** formulation of Maxwell's equations was used for modeling the superconductors. This is a computationally efficient modeling method developed specifically for REBCO tapes [8]. With this approach, the current vector potential, **T**, is applied to infinitely thin 1-D lines representing the HTS tapes, while the magnetic vector potential, **A**, is solved everywhere. The **T-A** formulation's applicability to HTS machine modeling has been previously validated in several articles [9], [12], [41].

A uniform mesh distribution of 50 elements was used for the **T**-formulated superconductors, and the discretization was set to linear for **T** and quadratic for **A**. Both the current and the magnet remanent flux density was ramped up from zero to obtain initial convergence. The simulations were run on Dell Poweredge C6420 computing nodes on NTNU's IDUN cluster [42], resulting in a computation time of about eight h for the base design.

The superconductor loss density (p_{HTS}) in $\mathrm{W/m^3}$ was found through the dot product of the electric field **E** and current density **J** in each tape

$$p_{\mathrm{HTS}} = \mathbf{E} \cdot \mathbf{J}. \tag{2}$$

The losses per axial length (P_{HTS}) in $\mathrm{W/m}$ were found for one slot by integrating this over each HTS tape and multiplying with the thickness of the REBCO layer, δ, set to $1\,\mu\mathrm{m}$

$$P_{\mathrm{HTS}} = \delta \int p_{\mathrm{HTS}}\, dl. \tag{3}$$

To find the time-averaged losses, (3) was integrated over the third half-period to avoid including transient behavior. The average losses in the slot of phase B+ were multiplied by the active length (l_a) and the number of slots (N_s) to find the average HTS losses in the entire machine ($\dot{Q}_{\mathrm{HTS}}$) in W

$$\dot{Q}_{\mathrm{HTS}} = l_a N_s P_{\mathrm{HTS}}. \tag{4}$$

E. Modeling Assumptions and Simplifications

The following assumptions and simplifications were made in the finite element modeling and analysis.

1) Only the active machine part was modeled, neglecting end windings and passive components.
2) Only electromagnetic analysis was conducted. Nonelectromagnetic materials were modeled as air.
3) The REBCO layer was modeled as an infinitely thin strip. NonSC layers were neglected.
4) All strands and filaments were modeled as perfectly uncoupled. An equal current was imposed on each one, neglecting coupling currents.
5) The HTS were assumed to have a uniform temperature and uniform material properties.
6) Only steady-state analysis was conducted.
7) Perfectly sinusoidal current without harmonics was set in the q-axis.

IV. HTS Loss Analysis

This section analyzes ac losses in the superconductors. First, a *base design* is studied, which has the parameters presented thus far. Then, losses at different conditions are studied before alterations are made to the design itself, investigating the impact on ac losses of: varying the normalized HTS peak current ($I_{\mathrm{peak}}/I_{c,\mathrm{s.f.}}$) through the number of strands per turn, aligning the HTS with the slot leakage flux, dividing the HTS into multiple filaments. Finally, it is studied how an HTS critical current improvement would impact the ac losses in this case.

A. Base Design Analysis

The *base design* is here defined as the machine and coil geometry given in Table I at full load, $5000\,\mathrm{r/min}$, and a temperature of 40 K in the superconductors. For this case, the instantaneous losses were found for all three slots in the model and plotted at steady-state in Fig. 7. As initially mentioned, the losses in each phase are symmetric and phase-shifted. Therefore, only the slot with phase B+ is investigated from this point.

A high alternating magnetic field over the HTS should be avoided since it has such a large impact on the ac losses. According to Ampere's law, the slot leakage flux is proportional to the current within the slot, and inversely proportional to the slot width [43], meaning that the peak SC current coincides with the peak field, as seen in Fig. 8. The maximum perpendicular and parallel field across the SCs is 0.60 and 1.27 T, respectively. The flux increases toward the slot top, and the turns closest to the air gap experience the highest magnetic field. Further, the flux is slightly inclined in the rotation direction due to the q-axis current.

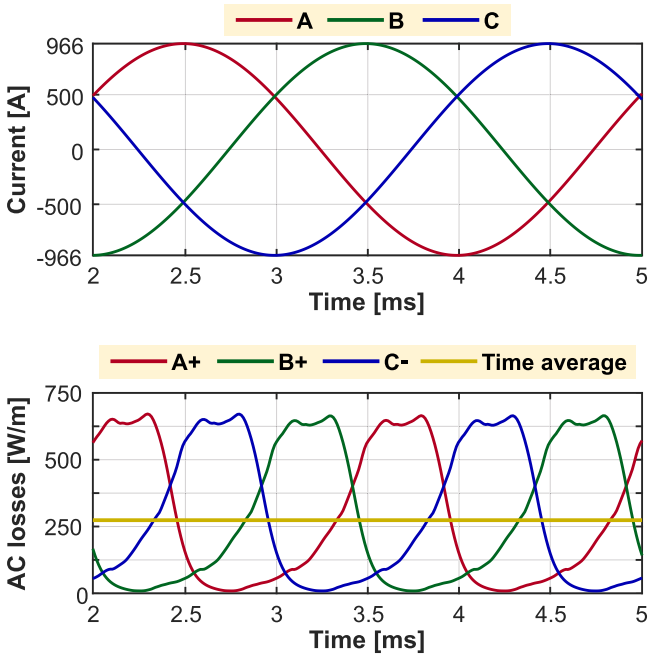

Fig. 7. Applied current and steady-state ac losses for one electrical period in a single slot for each phase found through 2-D FEA modeling of the HTS coil.

In Fig. 9, the normalized current density, $J/J_c(B)$, is plotted for the time instant, at which peak losses occur. Here, the net current is positive (red), and the negative current (blue) indicates shielding currents opposing the external perpendicular field. A relatively large portion of the conductors is shown to be inactive, i.e., without any current flowing in either direction. In the same figure, the loss density at peak losses is plotted along with the time-averaged loss density. The current and loss dissipation are both highest at the outer edges of the Roebel cable, with an asymmetry giving higher losses on the bottom side, coinciding with the asymmetry in the magnetic field (see Fig. 8). The total losses per turn are plotted against time in Fig. 10 for half an electrical period, where it can be observed that the outermost turns have the highest losses due to the higher external field.

B. Impact of Torque Loading

An aviation motor operates at full load at takeoff and during a shorter portion of the climb phase. At cruise, the load for a regional aircraft will typically be around 60%, while it is even lower for the descent and landing [44]. The output power is governed by speed and torque through the equation

$$P_{\text{mech}} = 2\pi \frac{n}{60} T. \tag{5}$$

In this analysis, the speed was kept constant at 5000 r/min, while the torque was reduced through the applied current. Fig. 11 shows the resulting ac losses normalized with respect to full-load losses, as well as the magnetic field and normalized current density in turn eight at peak losses. The figure shows that reducing the torque loading to 85% cuts the losses in half, while we see only 13.7% losses at 60% load. Hence, the combination of a reduced transport current and consequently a lower magnetic field is shown to give a substantial ac loss reduction for the slotted armature, meaning that ac losses can be significantly lowered for a large part of the flight. Also, it is evident that designs with lower ac losses are possible if allowing lower torque densities.

TABLE III
HTS LOSSES WHEN VARYING THE TEMPERATURE, WITH 40 K AS REFERENCE (SHOWN IN BOLD)

Temperature (K)	P_{tot}(W/m)	$\dot{Q}_{HTS}$ (W)	Increase (%)
25	153.6	885	-43.8
30	179.5	1034	-34.1
40	**273.3**	**1574**	**0.0**
50	448.0	2580	63.9
60	773.4	4455	183.0

TABLE IV
HTS LOSSES WHEN VARYING THE NUMBER OF STRANDS IN ROEBEL CABLE, WITH 18 STRANDS AS REFERENCE (SHOWN IN BOLD)

Strands	$I_{peak}/I_{c,s.f.}$ (%)	P_{HTS} (W/m)	Increase (%)
8	25.0	659.9	141.5
10	20.0	488.0	78.5
12	16.7	397.2	45.3
14	14.3	340.8	24.7
16	12.5	304.0	11.2
18	**11.1**	**273.3**	**0.0**
20	10.0	250.5	-8.3

C. Temperature Dependency of AC Losses

Using curve fits for the HTS critical current and power-law index at different temperatures, the temperature dependency of the HTS losses was found. Table III tabulates that the HTS temperature has a large impact on the losses, and keeping the temperature at 40 K or below is preferential. Still, because of different characteristics, this dependence will vary significantly between different HTS materials and suppliers. In addition, lowering the temperature can increase nonSC layer losses due to reduced resistivity [45]. In any case, the large temperature dependency illustrates the importance of an accurate HTS temperature estimation.

D. Effect of Number of Strands in Roebel Cable

In Fig. 9, a relatively large portion of the superconductors was found to carry close to zero current. To investigate whether the superconductors could be utilized better, the number of parallel strands per turn in the Roebel cable was varied. In the analysis, the turn center was kept at a constant location by increasing the distance between turns. The rest of the geometric entities were kept constant, while applying a constant current per turn. This way, superconductors were exposed to a comparable external field in each case, while effectively varying the normalized current (I/I_c). This led to the normalized current density shown in Fig. 12, and the corresponding total ac loss increase (compared with 18 strands) in Table IV.

Reducing the number of strands per turn can reduce the coil height slightly, and as such the required slot height, slightly reducing the machine weight. However, since much of the slot space, in this case, is reserved for cooling and thermal insulation,

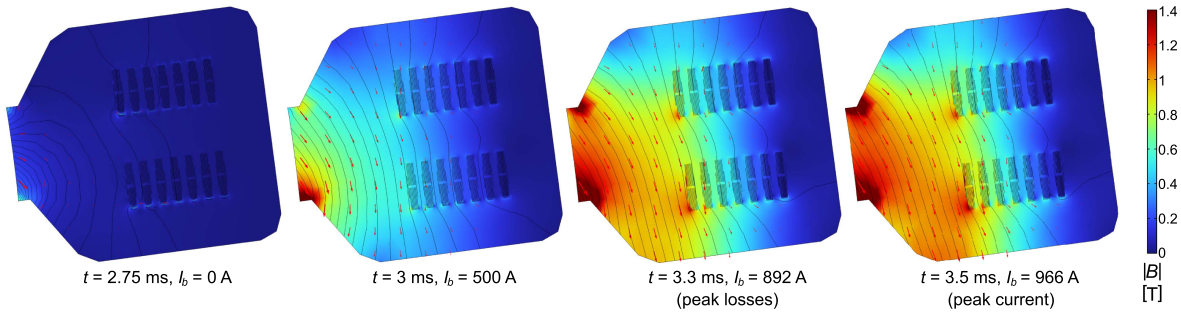

Fig. 8. Magnetic field in the slot with phase B+ at selected time instants, showing how slot flux covaries with current.

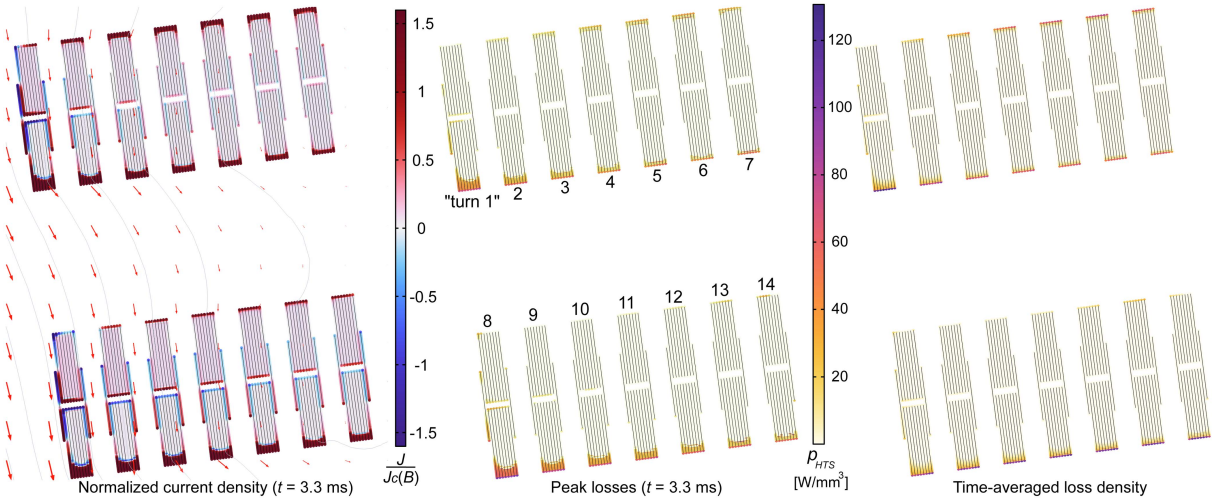

Fig. 9. Left: HTS normalized current density at the time-instant with peak losses. Middle: HTS loss density at the time-instant with peak losses. Right: Time-averaged HTS loss density in the slot with phase B+ at 40 K, 5000 r/min.

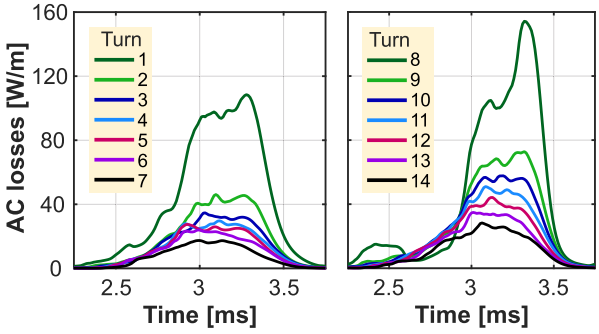

Fig. 10. Instantaneous losses (W/m) in the different turns in phase B+ at 40 K, 5000 r/min. Turn numbering is based on Fig. 3, where turns one and eight are the ones closest to the air gap.

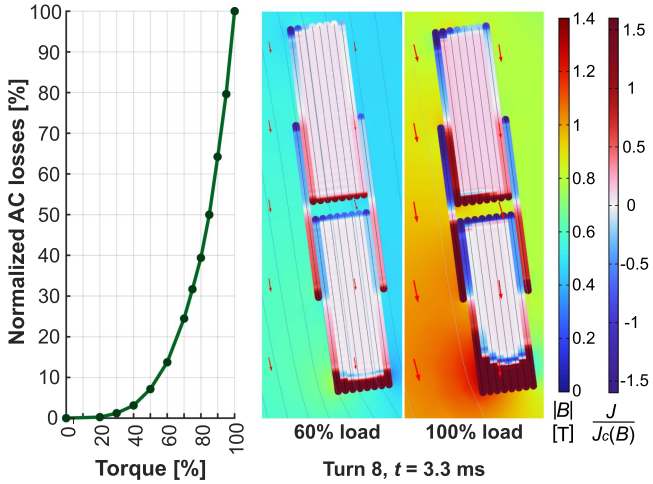

Fig. 11. Left: Time-averaged HTS losses at 40 K, 5000 r/min, normalized with respect to losses at full load (1574 W). Right: Magnetic field and normalized current density in turn eight at 60% and 100% of full load torque at $t = 3.3$ ms.

this has a small impact on the power density. When taking the ac losses in Table IV into account, it becomes clear that a relatively low normalized HTS peak current is beneficial for this design, and the number of strands per turn should not be reduced.

E. Impact of HTS Field Alignment

Because of the high aspect ratio (width/height) of the superconductors, an alternating magnetic field perpendicular to the tape surface will induce Eddy currents. Aligning the tapes with the external field has been shown to effectively reduce the losses [46]. Initially, the superconductors were parallel with the slot bottom, while the field was found to be slightly inclined in

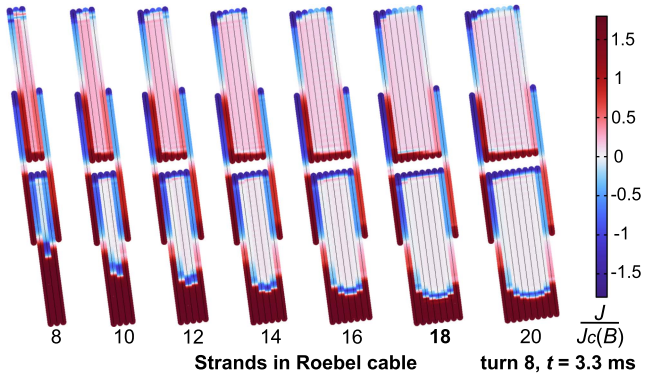

Fig. 12. Normalized current density in turn eight at $t = 3.3$ ms when varying the number of strands in Roebel cable.

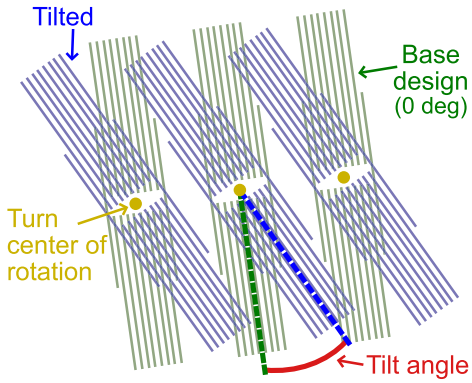

Fig. 13. Illustration of counterclockwise HTS tilt. The base design, where the HTS are parallel with the slot bottom is considered as the reference (0°). Each turn is rotated separately with respect to its geometric centre.

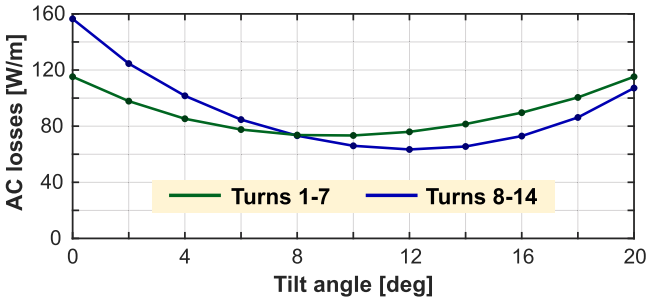

Fig. 14. Time-averaged ac losses in the two coilsides when tilting each turn with a resolution of 2°.

the rotation direction (see Fig. 8). To align the HTS with the field, while keeping the coil in place, each Roebel cable turn was tilted counterclockwise relative to the turn centre as shown in Fig. 13. In each coilside, all turns were tilted by an equal amount.

In Fig 14, we see that the optimal configuration would be to tilt the two coilsides with 10° and 12°, respectively. Doing this would give an ac loss of 788 W for the entire machine, about half of the losses in the base design. The maximum perpendicular flux over the SCs is now reduced to 0.47 T. A plot of the magnetic field and normalized current density is given in Fig. 15 for this case. From this figure, it can be observed that the current is

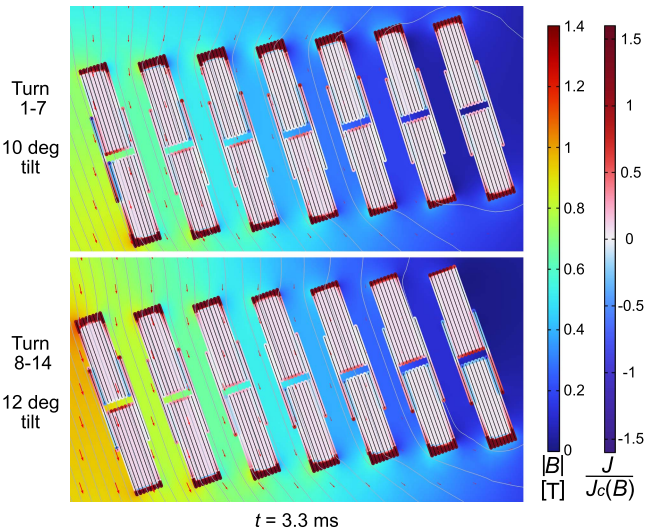

Fig. 15. Magnetic field and normalized current density with optimal tilt angles for the two coilsides at $t = 3.3$ ms.

TABLE V
TIME-AVERAGED HTS LOSSES WHEN VARYING THE NUMBER OF FILAMENTS

N_{fil}	W_{fil} (μm)	P_{HTS} (W/m)	Increase (%)
1	1900.0	273.3	0
2	925.0	370.4	35.5
4	437.5	427.3	56.3
6	275.0	395.7	44.8
8	193.8	349.2	27.8
10	145.0	280.4	2.6
15	80.0	152.4	-44.2
20	47.5	79.3	-71.0

almost unidirectional, meaning that shielding currents have been reduced compared with the base design. It should be noted that this loss reduction is specific both with regards to the rotation direction and the q-axis current. Further, tilting the HTS might complicate the end winding shape, and affect the mechanical support and cooling within the slot.

F. Impact of Filamentization

Filamentization is another way to reduce HTS Eddy currents from alternating perpendicular fields. By cutting the tape into multiple narrow filaments, the effective dimension of the superconductor perpendicular to the magnetic field can be reduced. In theory, this can reduce magnetizing losses by a factor equal to the number of filaments [47]. The filaments are separated by grooves, typically between 20–100 μm, to have a sufficiently large matrix resistivity to avoid high coupling currents [29].

In this section, it is investigated whether filamentization is a loss reduction technique well suited for this design. The groove width was set to 50 μm, and the reduction in tape width due to grooves is taken into account for the critical current. A gradient mesh (see [11]) with 35, 25, 20, 15, 15, 12, and 10 elements was used for the 2, 4, 6, 8, 10, 15, and 20 filaments, respectively.

Varying the number of filaments per strand resulted in the losses given in Table V. Here, the losses *increased* for ten filaments or less, even when coupling losses between filaments

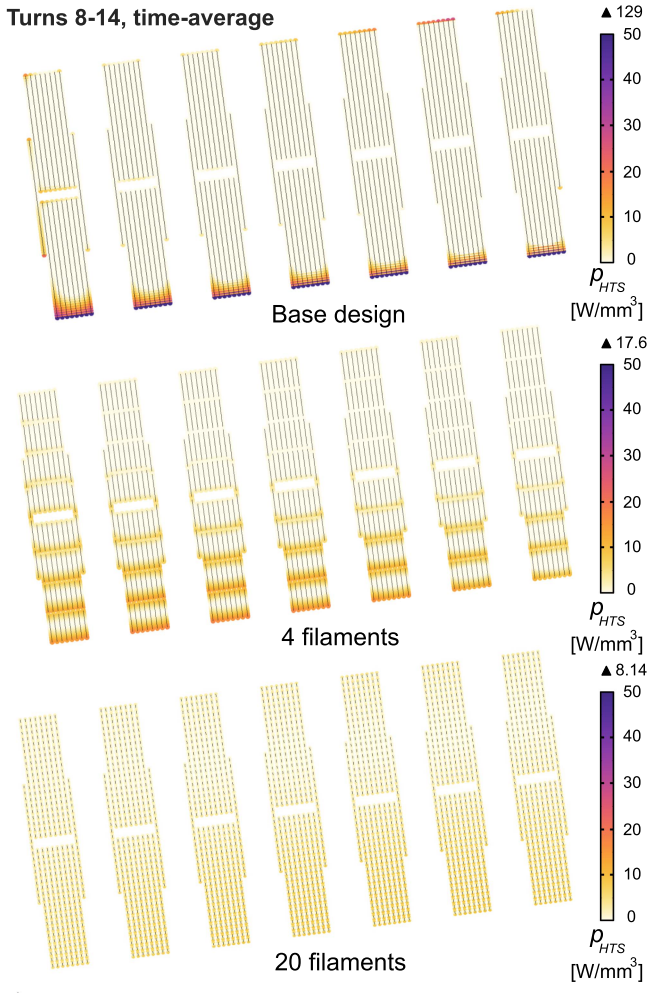

Fig. 16. Time-averaged HTS loss density in turns 8–14 for the base design, four filaments and 20 filaments. The range was set manually in all cases to have a comparable color legend. The maximum value in each case is indicated in the respective legends.

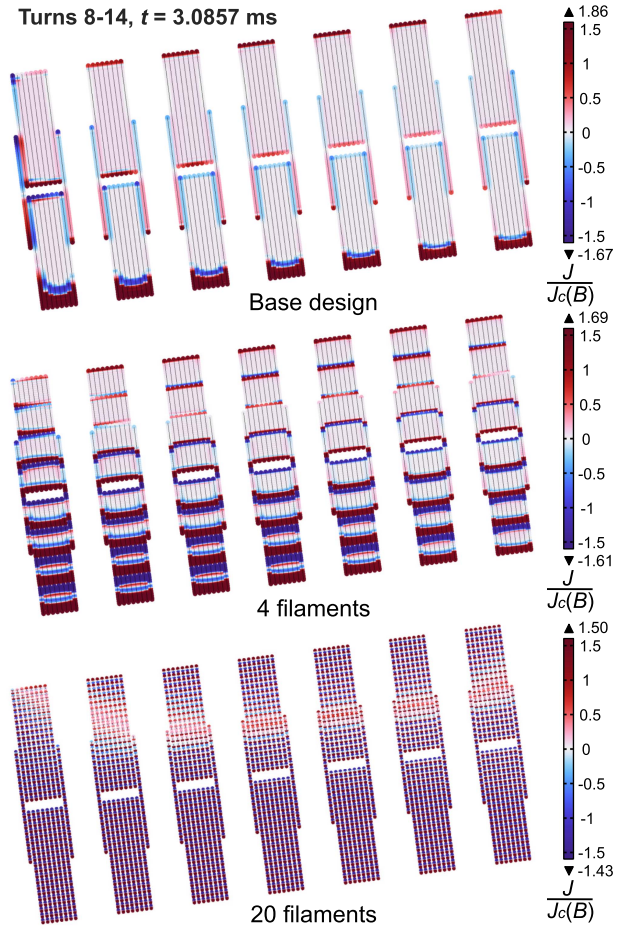

Fig. 17. Normalized current density in turns 8–14 at $t = 3.0857$ ms for the base design, four filaments, and 20 filaments. The range was set manually in all cases to have a comparable color legend. The maximum and minimum value in each case is indicated in the respective legends.

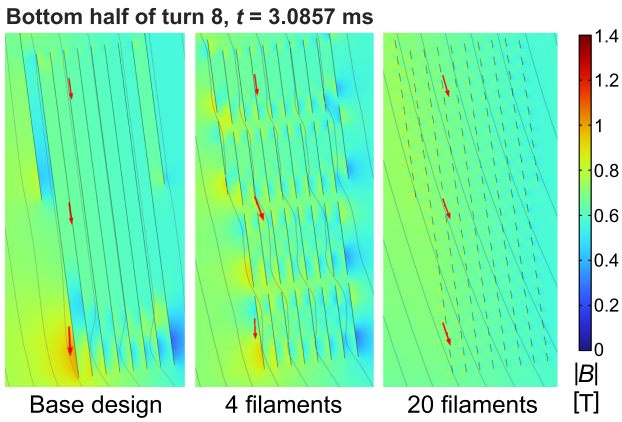

Fig. 18. Magnetic field in the bottom half of turn eight at $t = 3.0857$ ms for the base design, four filaments, and 20 filaments.

are not considered. Fig. 16 shows that the time-averaged loss density in the original case was very high only at the outermost edges of the tapes, while the losses are more evenly distributed within the multifilamentary tapes with a much lower peak loss density. Similar observations can be made for the normalized current density in Fig. 17. An explanation for this might be that the magnetic field induces shielding currents in the SCs. When investigating the magnetic field in Fig. 18, we find that the shielding seems to be more effective for the nonfilamentary case, protecting a larger SC-volume from the perpendicular field at the cost of a higher peak current on the tape edges. For four filaments, the shielding effect is still there, albeit not as effective as the original case. For 20 filaments, the shielding effect is much weaker, seeing how the flux lines are almost unaffected by the HTS. The proximity effect is likely playing a part here, and might be stronger for few filaments due to a larger current capacity within each filament.

The analysis suggests that many filaments are needed in order to have a worthwhile impact on the ac losses. While the loss reduction potential of 20 filaments looks very promising, several downsides must be kept in mind. Producing too narrow filaments in long conductors is risky since this increases the likelihood of defects in different filaments, potentially blocking the current path [47]. Furthermore, the filamentization process reduces the critical current beyond the loss of HTS-material,

TABLE VI
HTS LOSSES WHEN INCREASING THE CRITICAL CURRENT

k	$I_{peak}/I_{c,s.f.}$ (%)	P_{HTS} (W/m)	Reduction (%)
1	11.1	273.3	0.0
1.5	7.41	170.9	37.5
2	5.56	140.0	48.8
3	3.70	102.2	62.6
4	2.78	81.2	70.3

due to material inhomogeneity and possible damage from laser ablation [48]. Also, it degrades mechanical strength [49], and coupling losses between filaments can be substantial, especially at higher frequencies [47]. It should be noted that filamentization is a more effective loss reduction measure when the external field has a larger perpendicular component, as shown in [11].

G. Impact of Critical Current Improvement

Recently, REBCO HTS has undergone rapid development and entered the stage of early commercialization, where multiple actors can supply long lengths with a relatively high critical current. We might see HTS with even higher critical current density in the years to come, through improving artificial pinning or increasing the thickness of the REBCO layer [50]. For example, the commercially available HTS used in this analysis had a self-field critical current per width of $648\,\mathrm{A/cm}$ at a temperature of $77\,\mathrm{K}$, while works, such as Kim et al. [51], achieved over $1500\,\mathrm{A/cm}$ for a short sample [51]. Therefore, a short investigation was made on how further improvements would help reduce losses in the given design. This was done by using the same field dependence curves as in Fig. 6 while increasing the self-field critical current by a given factor, k. When increasing the critical current, a larger portion of the current accumulates at the very edges of the tapes. To capture this, a gradient mesh (see [11]) with 50, 50, 70, and 90 elements was used for $k = 1.5$, 2, 3, and 4, respectively. The results are given in Table VI, where doubling the critical current is shown to almost halve the losses.

V. DESIGN EVALUATION AND DISCUSSION

In this section, an overview of the machine's performance is presented before a discussion part containing a brief comparison with the SotA for conventional machines as well as some of the study limitations.

A. Machine Performance Overview

Table VII gives an overview of parameters related to the machine performance at full load operation with an HTS temperature of 40 K and optimal HTS field alignment (see Section IV-E). With the exception of HTS losses, the results were found with an overview model with lossless coils given in Fig. 5. From these results, it can be seen that the cryogenic cooling requirement was estimated to be 1188 W, or 0.0475% of the output power, for full-load operation at 40 K. While this is likely an underestimate, as will be further discussed, it shows that this machine has potential as a highly efficient alternative to conventional machines with a low enough cooling requirement to encourage further development and research on the unsolved aspects of the design. The torque density might be high enough to warrant direct drive operation, but a detailed analysis of the cooling system is required to get a good estimate of the weight of passive components.

The magnetic flux density for $t = 0$ s is shown in Fig. 19. At this time instant, the flux in the middle slot is at its maximum. The steel is saturated both in the teeth and yoke. As previously discussed, it can be observed that the flux has a slight asymmetry because of the q-axis current, particularly in the tooth shoes, which are over-saturated. The q-axis current alignment

TABLE VII
PERFORMANCE PARAMETERS OF FINAL MACHINE DESIGN WITH HTS OPERATING AT 40 K WITH OPTIMAL TILT ANGLE

Parameter	Symbol	Value	Unit
Average mechanical power	P_{mech}	2500	kW
Rotational speed	n	5000	r/min
Electrical frequency	f_{el}	333.3	Hz
Phase voltage (rms)	U_{ph}	421	V
Back-emf fundamental (rms)	$E_{\mathrm{ph},1}$	313	V
Applied phase current (rms)	I_{ph}	683	A
Peak current per 1.9 mm strand	$I_{\mathrm{peak,strand}}$	53.7	A
Normalized HTS peak current	$I_{\mathrm{peak}}/I_{\mathrm{c,s.f.}}$	11.1	%
Useful slot current density (rms)	J_{us}	28.1	A/mm^2
Synchronous inductance	L_{ph}	0.415	pu
Base inductance	L_b	294	µH
Power factor	$\cos(\phi)$	0.725	
Average torque	T	4776	Nm
Torque ripple	ΔT	3.17	%
Steel weight	m_{fe}	57.7	kg
Magnet weight	m_{pm}	26.9	kg
Slot weight	m_s	9.3[I]	kg
Active weight	m_{act}	93.9	kg
Active power density	PTW_{act}	26.6	kW/kg
Active torque density	TTW_{act}	50.9	Nm/kg
Steel losses	$\dot{Q}_{\mathrm{steel}}$	1497	W
PM losses	$\dot{Q}_{\mathrm{PM}}$	1943	W
Active HTS ac losses[II]	$\dot{Q}_{\mathrm{HTS}}$	788[III]	W
Heat leak into slots[IV]	$\dot{Q}_{\mathrm{leak}}$	400	W
Cryogenic cooling requirement	$\dot{Q}_{\mathrm{cryo}}$	1188	W
Efficiency estimate[V]	η	99.8	%

[I] Assuming density of 4000 kg/m^3 for slot.
[II] In REBCO layer only. Not including end windings, coupling losses or eddy losses in nonSC layers.
[III] Full load at 40 K with optimal tilt (see section IV-E).
[IV] Rough estimation from section II-C.
[V] Not considering a cooling penalty related to cryogenic heat removal.

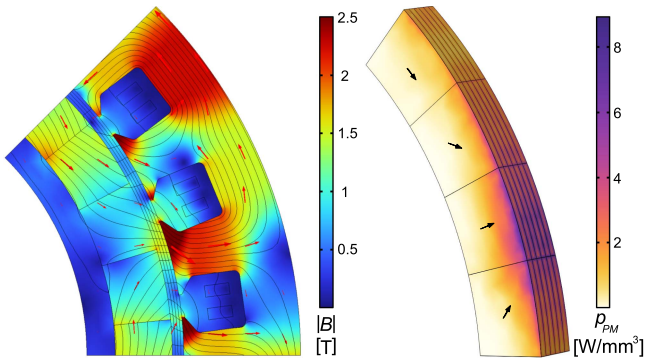

Fig. 19. Left: Magnetic flux density at full load and $t = 0$ s. Right: Time-averaged PM loss density for six axial segments of 2 mm.

TABLE VIII
KEY PERFORMANCE PARAMETERS

Parameter	Slotted HTS armature	Golovanov *et al.* [25]	Unit
Mechanical power	2500	4000	kW
Speed	5000	15000	r/min
Active power density	26.6	35.4	kW/kg
Active torque density	50.9	22.5	Nm/kg
Slot current density	28.1	≈20	A/mm^2
Efficiency estimate	99.8	98.3	%

also gives a relatively low power factor, increasing the size of the converter since it must supply the resulting reactive power requirement. A time-domain formulation of Bertotti's loss equation given in [52] was used to estimate the steel losses, of which the hysteresis, excess and Eddy current loss components amounted to 772, 255, and 470 W, respectively.

PM Eddy losses were found by extruding a model with lossless coils axially into 3-D with segments of 2 mm in the axial direction, all assumed to be electrically insulated from one another. The end effect was accounted for by an external air domain and an additional coil length of 1 mm on the axial end of the machine. This resulted in total PM-losses of 1943 W with the loss distribution shown for six axial segments in Fig. 19. In the PMs, the minimum flux in the magnetization direction was found to go down to -0.05 T in the innermost part of the outward-facing magnet. Hence, the magnets must be kept below ca. 150 °C to avoid demagnetization [53], [54]. This could be improved by having a rotor back-iron, but optimizing the rotor design has been considered out of scope for this article.

B. Tradeoffs Compared with SotA and Other Design Choices

Conventional electrical machines can also reach high power densities through high-speed design. For example, Golovanov et al. [25] did an optimization study of a design with a Halbach array rotor and slotted stator with copper windings. In this work, this was considered the SotA for electric aviation machines, and in Table VIII its key performance parameters are compared with the ones for this article's machine.

When only considering active parts, Golovanov's machine has a superior power density since it is designed for a higher rotational speed. If comparing the speed-independent torque density instead, the superconducting machine is over twice as torque-dense. However, when comparing the two designs, there are many nuances to consider. For example, considering only the active parts is a large simplification. Nevertheless, the immaturity of superconducting machines makes it more difficult to make an accurate estimate for passive components, such as the cooling loop. Also, high-speed designs lead to increased friction and windage losses, in addition to the need for a gearbox if the machine is used as a propulsive motor, further increasing system losses and weight. Moreover, a higher efficiency could also cut weight through a lower power and energy demand for the entire drivetrain.

In this slotted design with warm steel, much of the slot space is reserved for thermal insulation, resulting in a coil area (68 mm^2) of only a fifth of the useful slot area (340 mm^2), which leads to a relatively low current density in the useful slot of this design (28.1 A/mm^2), not significantly higher than Golovanov's conventional design (ca. 20 A/mm^2). Other topologies or design choices, such as a slotless stator or a cryogenic steel, could improve the power density but would almost certainly increase the required cooling. For now, the true challenge and constraint is to limit the ac losses sufficiently to be able to keep the HTS coils at cryogenic temperature. The same reasoning also applies to the normalized HTS peak current ($I_{\text{peak}}/I_{c,s.f.}$), for which it can be argued that 11.1% is low, not fully utilizing the superconductor material. However, as shown in Section IV-D, maintaining the same current, while reducing the number of parallel coupled HTS tapes increases losses significantly, while having a minimal impact on power density since most of the slot space is occupied by the thermal insulation.

C. Study Limitations

The ac loss estimate is most likely too low since it only considered the REBCO layer in the active part of the machine. Eddy losses in nonSC layers were not considered, and in [55], losses in the copper stabilizer amounted to ca. 20% of the total magnetization losses in a single tape at a frequency of 333 Hz. This portion is likely not the same in the analyzed machine due to a more complex geometry and magnetic field, in addition to the HTS transport current. Hence, it is clear that losses in the copper stabilizer must be examined with a multilayer model like in [56]. The applied current was modeled as perfectly sinusoidal, and loss increase from current harmonics was not examined. Further, cold losses, as well as heat leaks in the end-winding and current leads, have not been included in this analysis, and the total cryogenic cooling requirement will be significantly higher. On the other hand, it was shown that the torque loading has a large impact on the ac losses of the HTS coil (see Fig. 11), and in other flight phases than takeoff, the losses can be significantly lowered. Nonetheless, the magnitude of the losses indicates that a cryocooler is unsuitable for this application due to its cooling penalty and weight, and an LH_2 cooling system is most likely needed to make an HTS armature an attractive alternative for aviation motors.

In all analyses, the HTS tapes were modeled as perfectly uncoupled, each with an equal net current justified by the Roebel cable transposition. Still, coupling currents could be present, increasing HTS losses and influencing the current distribution within the Roebel cable. Especially when analyzing the effect of filamentization, this might introduce an error since the filaments are not fully transposed.

The overall machine design and performance is based on the assumption that it fits a cryogenic cooling system able to maintain the specified HTS temperatures. To demonstrate the design feasibility, a detailed study of the cooling system must be conducted using ac loss estimates from this article. Also, end windings of a distributed winding are longer and more complex than the concentrated windings dominating the HTS literature, necessitating an investigation of their cooling and thermal insulation.

VI. Conclusion

In this article, a power-dense $2.5\,\mathrm{MW}$ electric aviation motor with a slotted HTS armature and Halbach array rotor was designed and analyzed. Its figures-of-merit demonstrate a high technical potential with an electric efficiency of 99.8% and an active torque density of 50.9 N·m/kg. The required cryogenic cooling was approximated to about 0.05% of the output power at $40\,\mathrm{K}$ but is likely underestimated due to simplifications made in the analysis.

A comprehensive ac loss analysis of the HTS coil configuration was conducted. This showed that the major share of the ac losses is highest in the outermost turns, where the slot leakage flux is highest. The losses are highly dependent on the torque loading of the machine since increasing the transport current also contributes to higher slot leakage flux. Consequently, in other flight phases than takeoff, the ac losses can be very low. The temperature dependency of the HTS REBCO layer's ac losses was shown, and the impact of the normalized HTS peak current was investigated by varying the number of strands per Roebel cable turn.

High-precision alignment of the HTS tapes with respect to the slot leakage flux was shown to be an effective loss reduction measure, roughly halving the losses with a 10° tilt difference. On the other hand, it is clear that filamentization does not warrant an ac loss reduction in all cases. While a large number of filaments indicated an efficient loss reduction, fewer than ten filaments was shown to actually increase losses, showing that extra care should be taken when considering multifilamentary tapes in cases where the field is not directly perpendicular to the HTS tapes. Assuming a twofold increase in critical current performance of the HTS tape, the ac losses were nearly halved, illustrating the potential for further HTS material advancements.

Still, key aspects of the design remain unexamined. A more thorough analysis of the cryogenic cooling requirement is recommended since ac losses related to current harmonics, coupling, end windings, and Eddy currents in the nonSC layers were not considered. The heat leak should also be examined more closely, not only in the slots but also in the end windings and current leads, and a detailed design of the cryogenic cooling loop is also necessary to make further conclusions on the feasibility of the HTS armature winding. Finally, a thorough examination of operational safety and quench protection must be conducted.

References

[1] D. Lee et al., "The contribution of global aviation to anthropogenic climate forcing for 2000 to 2018," *Atmos. Environ.*, vol. 244, pp. 117834–117834, 2021.

[2] P. J. Masson, G. V. Brown, D. S. Soban, and C. A. Luongo, "HTS machines as enabling technology for all-electric airborne vehicles," *Supercond. Sci. Technol.*, vol. 20, no. 8, Jun. 2007, Art. no. 748.

[3] M. Gouge, J. Demko, B. Mcconnell, and J. Pfotenhauer, "Cryogenics assessment report," Oak Ridge, TN, USA: Oak Ridge Nat. Lab., 2002.

[4] C. C. Chow, M. D. Ainslie, and K. Chau, "High temperature superconducting rotating electrical machines: An overview," *Energy Rep.*, vol. 9, pp. 1124–1156, 2023.

[5] K. S. Haran et al., "High power density superconducting rotating machines–development status and technology roadmap," *Supercond. Sci. Technol.*, vol. 30, no. 12, Nov. 2017, Art. no. 123002.

[6] J. K. Nøland, R. Mellerud, and C. Hartmann, "Next-generation cryo-electric hydrogen-powered aviation: A disruptive superconducting propulsion system cooled by onboard cryogenic fuels," *IEEE Ind. Electron. Mag.*, vol. 16, no. 4, pp. 6–15, Dec. 2022.

[7] C. Hartmann, J. K. Nøland, R. Nilssen, and R. Mellerud, "Dual use of liquid hydrogen in a next-generation PEMFC-powered regional aircraft with superconducting propulsion," *IEEE Trans. Transport. Electrific.*, vol. 8, no. 4, pp. 4760–4778, Dec. 2022.

[8] F. Huber, W. Song, M. Zhang, and F. Grilli, "The T-A formulation: An efficient approach to model the macroscopic electromagnetic behaviour of HTS coated conductor applications," *Supercond. Sci. Technol.*, vol. 35, no. 4, 2022, Art. no. 043003.

[9] T. Benkel et al., "T–A-formulation to model electrical machines with HTS coated conductor coils," *IEEE Trans. Appl. Supercond.*, vol. 30, no. 6Sep. 2020, Art. no. 5205807.

[10] S. You, S. Kalsi, M. D. Ainslie, R. A. Badcock, N. J. Long, and Z. Jiang, "Numerical simulation of AC loss in the armature windings of two 50 kW-class ALL-HTS motors with different pole shapes," *IEEE Trans. Appl. Supercond.*, vol. 32, no. 4, Jun. 2022, Art. no. 5200307.

[11] S. You, S. S. Kalsi, M. D. Ainslie, R. A. Badcock, N. J. Long, and Z. Jiang, "Simulation of AC loss in the armature windings of a 100 kW all-HTS motor with various (RE)BCO conductor considerations," *IEEE Access*, vol. 9, pp. 130968–130980, 2021.

[12] C. R. Vargas-Llanos, S. Lengsfeld, and F. Grilli, "T-A formulation for the design and AC loss calculation of a superconducting generator for a 10 MW wind turbine," *IEEE Access*, vol. 8, pp. 208767–208778, 2020.

[13] F. Grilli et al., "Superconducting motors for aircraft propulsion: The advanced superconducting motor experimental demonstrator project," *J. Phys. Conf. Ser.*, vol. 1590, no. 1, 2020, Art. no. 012051.

[14] M. Corduan, M. Boll, R. Bause, M. P. Oomen, M. Filipenko, and M. Noe, "Topology comparison of superconducting AC machines for hybrid electric aircraft," *IEEE Trans. Appl. Supercond.*, vol. 30, no. 2, Mar. 2020, Art. no. 5200810.

[15] N. Ivanov et al., "Calculation, design, and winding preliminary tests of 90-kW HTS machine for small-scale demonstrator of generating system for future aircraft with hybrid propulsion system," *IEEE Trans. Appl. Supercond.*, vol. 33, no. 2, Mar. 2023, Art. no. 5200105.

[16] S. S. Kalsi, R. A. Badcock, J. G. Storey, K. A. Hamilton, and Z. Jiang, "Motors employing REBCO CORC and MgB_2 superconductors for AC stator windings," *IEEE Trans. Appl. Supercond.*, vol. 31, no. 9, Dec. 2021, Art. no. 5206807.

[17] F. Weng, M. Zhang, T. Lan, Y. Wang, and W. Yuan, "Fully superconducting machine for electric aircraft propulsion: Study of AC loss for HTS stator," *Supercond. Sci. Technol.*, vol. 33, no. 10, Aug. 2020, Art. no. 104002.

[18] B. Oswald et al., "Project SUTOR superconducting speed-controlled torque motor for 25.000 nm," *Phys. Procedia*, vol. 36, pp. 765–770, 2012.

[19] S. Fukuda et al., "Design study of 2-MW fully superconducting synchronous motors," *IEEE Trans. Appl. Supercond.*, vol. 28, no. 4, Jun. 2018, Art. no. 5207806.

[20] R. Sugouchi et al., "Conceptual design and electromagnetic analysis of 2 MW fully superconducting synchronous motors with superconducting magnetic shields for turbo-electric propulsion system," *IEEE Trans. Appl. Supercond.*, vol. 30, no. 4, Jun. 2020, Art. no. 3601905.

[21] D. S. Dezhin and I. N. Dezhina, "Development of the future aircraft propulsion system based on HTS electrical equipment with liquid hydrogen cooling," *IEEE Trans. Appl. Supercond.*, vol. 32, no. 4, Jun. 2022, Art. no. 3601105.

[22] U. Shipurkar, H. Polinder, and J. A. Ferreira, "Modularity in wind türbine generator systems – Opportunities and challenges," in *Proc. Eur. Conf. Power Electron. Appl.*, 2016, pp. 1–10.

[23] R. Mellerud, J. Nøland, and C. Hartmann, "Preliminary design of a 2.5-MW superconducting propulsion motor for hydrogen-powered aviation," in *Proc. Int. Conf. Elect. Mach.*, 2022, pp. 1404–1410.

[24] D. Lee et al., "Design and prototype of a high power density slotless PMSM for direct drive aircraft propulsion," in *Proc. IEEE Power Energy Conf. Illinois*, 2021, pp. 1–6.

[25] D. Golovanov et al., "4-MW class high-power-density generator for future hybrid-electric aircraft," *IEEE Trans. Transport. Electrific.*, vol. 7, no. 4, pp. 2952–2964, Dec. 2021.

[26] D. Golovanov, D. Gerada, Z. Xu, C. Gerada, A. Page, and T. Sawata, "Designing an advanced electrical motor for propulsion of electric aircraft," in *Proc. IEEE/AIAA Electric Aircr. Technol. Symp.*, 2019, pp. 1–12.

[27] M. Filipenko et al., "Concept design of a high power superconducting generator for future hybrid-electric aircraft," *Supercond. Sci. Technol.*, vol. 33, no. 5, 2020, Art. no. 054002.

[28] W. Goldacker, F. Grilli, E. Pardo, A. Kario, S. I. Schlachter, and M. Vojenčiak, "Roebel cables from REBCO coated conductors: A one-century-old concept for the superconductivity of the future," *Supercond. Sci. Technol.*, vol. 27, no. 9, Aug. 2014, Art. no. 093001.

[29] A. Godfrin, "AC losses in high-temperature superconductor tapes and cables for power applications," Ph.D. dissertation, Karlsruher Institut Für Technologie, Karlsruhe, Germany, 2020.

[30] M. Nii, N. Amemiya, and T. Nakamura, "Three-dimensional model for numerical electromagnetic field analyses of coated superconductors and its application to Roebel cables," *Supercond. Sci. Technol.*, vol. 25, no. 9, Jul. 2012, Art. no. 095011.

[31] S. Wimbush, N. Strickland, and A. Pantoja, "Critical current characterisation of Shanghai superconductor low field high temperature 2G HTS superconducting wire," Feb. 2022. [Online] Available: https://figshare.com/articles/dataset/Critical_current_characterisation_of_Shanghai_Superconductor_Low_Field_High_Temperature_2G_HTS_superconducting_wire/19185092

[32] S. J. Otten, "Characterisation of REBCO Roebel cables," Ph.D. dissertation, Karlsruher Institut Für Technologie (KIT), Karlsruhe, Germany, 2019.

[33] L. Ybanez et al., "ASCEND: The first step towards cryogenic electric propulsion," *IOP Conf. Ser.: Mater. Sci. Eng.*, vol. 1241, no. 1, May 2022, Art. no. 012034.

[34] J. L. Felder, G. V. Brown, H. DaeKim, and J. Chu, "Turboelectric distributed propulsion in a hybrid wing body aircraft," in *Proc. 20th Int. Soc. Airbreathing Engines*, 2011, pp. 1–20.

[35] H. Sugimoto et al., "Development of an axial flux type PM synchronous motor with the liquid nitrogen cooled HTS armature windings," *IEEE Trans. Appl. Supercond.*, vol. 17, no. 2, pp. 1637–1640, Jun. 2007.

[36] D. Verstraete, P. Hendrick, P. Pilidis, and K. Ramsden, "Hydrogen fuel tanks for subsonic transport aircraft," *Int. J. Hydrogen Energy*, vol. 35, no. 20, pp. 11085–11098, Oct. 2010.

[37] M. Yazdani-Asrami, S. M. Seyyedbarzegar, M. Zhang, and W. Yuan, "Insulation materials and systems for superconducting powertrain devices in future cryo-electrified aircraft: Part I–material challenges and specifications, and device-level application," *IEEE Electr. Insul. Mag.*, vol. 38, no. 2, pp. 23–36, Mar. 2022.

[38] S. C. Wimbush and N. M. Strickland, "A public database of high-temperature superconductor critical current data," *IEEE Trans. Appl. Supercond.*, vol. 27, no. 4, Jun. 2017, Art. no. 8000105.

[39] K. P. Thakur et al., "Frequency-dependent critical current and transport ac loss of superconductor strip and Roebel cable," *Supercond. Sci. Technol.*, vol. 24, no. 6, 2011, Art. no. 065024.

[40] X. Zhang et al., "Study of critical current and n-values of 2G HTS tapes: Their magnetic field-angular dependence," *J. Supercond. Novel Magn.*, vol. 31, no. 12, pp. 3847–3854, 2018.

[41] Y. Yang, H. Yong, X. Zhang, and Y. Zhou, "Numerical simulation of superconducting generator based on the *T–A* formulation," *IEEE Trans. Appl. Supercond.*, vol. 30, no. 8, Dec. 2020, Art. no. 5207611.

[42] M. Själander, M. Jahre, G. Tufte, and N. Reissmann, "EPIC: An energy-efficient, high-performance GPGPU computing research infrastructure," 2022, *arXiv:1912.05848.*

[43] J. Pyrhönen, "Design of rotating electrical machines," 2nd ed. Hoboken, NJ, USA: Wiley, 2008.

[44] B. Jux, S. Foitzik, and M. Doppelbauer, "A standard mission profile for hybrid-electric regional aircraft based on web flight data," in *Proc. IEEE Int. Conf. Power Electron., Drives Energy Syst.*, 2018, pp. 1–6.

[45] F. Grilli, E. Pardo, A. Stenvall, D. N. Nguyen, W. Yuan, and F. Gömöry, "Computation of losses in HTS under the action of varying magnetic fields and currents," *IEEE Trans. Appl. Supercond.*, vol. 24, no. 1, Feb. 2014, Art. no. 8200433.

[46] C. R. Vargas-Llanos, S. Lengsfeld, M. Noe, T. Arndt, and F. Grilli, "Influence of coil position on AC losses of stator superconducting windings of a synchronous machine for a 10 MW wind turbine," *IEEE Trans. Appl. Supercond.*, vol. 31, no. 7, Oct. 2021, Art. no. 5206509.

[47] F. Grilli and A. Kario, "How filaments can reduce AC losses in HTS coated conductors: A review," *Supercond. Sci. Technol.*, vol. 29, no. 8, 2016, Art. no. 083002.

[48] A. Godfrin et al., "Influence of the striation process and the thickness of the Cu-stabilization on the AC magnetization loss of striated RE-BCO tape," *IEEE Trans. Appl. Supercond.*, vol. 27, no. 6, Sep. 2017, Art. no. 5900809.

[49] H. Zhang, Z. Wen, F. Grilli, K. Gyftakis, and M. Mueller, "Alternating current loss of superconductors applied to superconducting electrical machines," *Energies*, vol. 14, no. 8, 2021, Art. no. 2234.

[50] C. Yao and Y. Ma, "Superconducting materials: Challenges and opportunities for large-scale applications," *Iscience*, vol. 24, no. 6, 2021, Art. no. 102541.

[51] H. S. Kim et al., "Ultra-high performance, high-temperature superconducting wires via cost-effective, scalable, co-evaporation process," *Sci. Rep.*, vol. 4, 2014, Art. no. 4744.

[52] F. Fiorillo and A. Novikov, "An improved approach to power losses in magnetic laminations under nonsinusoidal induction waveform," *IEEE Trans. Magn.*, vol. 26, no. 5, pp. 2904–2910, Sep. 1990.

[53] Arnold Magnetic Technologies, "Gb46eh," Accessed: May 22, 2023. [Online] Available: https://www.arnoldmagnetics.com/wp-content/uploads/2021/07/GB46EH.pdf

[54] M. Galea, L. Papini, H. Zhang, C. Gerada, and T. Hamiti, "Demagnetization analysis for Halbach array configurations in electrical machines," *IEEE Trans. Magn.*, vol. 51, no. 9, Sep. 2015, Art. no. 8107309.

[55] H. Zhang et al., "Modelling of electromagnetic loss in HTS coated conductors over a wide frequency band," *Supercond. Sci. Technol.*, vol. 33, no. 2, 2020, Art. no. 025004.

[56] H. Zhang, P. Machura, K. Kails, H. Chen, and M. Mueller, "Dynamic loss and magnetization loss of HTS coated conductors, stacks, and coils for high-speed synchronous machines," *Supercond. Sci. Technol.*, vol. 33, no. 8, 2020, Art. no. 084008.